# Surface plasmon lasers

Tenner, V.T.

**Citation**

Tenner, V. T. (2017, June 22). *Surface plasmon lasers*. *Casimir PhD Series*. Retrieved from https://hdl.handle.net/1887/49932

Cover Page

# Universiteit Leiden

**Author:** Tenner, V.T.
**Title:** Surface plasmon lasers
**Issue Date:** 2017-06-22

# Surface plasmon dispersion in metal hole array lasers

We experimentally study surface plasmon lasing in a series of metal hole arrays on a gold-semiconductor interface. The sub-wavelength holes are arranged in square arrays of which we systematically vary the lattice constant and hole size. The semiconductor medium is optically pumped and operates at telecom wavelengths ($\lambda \sim 1.5~\mu m$). For all 9 studied arrays, we observe surface plasmon (SP) lasing close to normal incidence, where different lasers operate in different plasmonic bands and at different wavelengths. Angle- and frequency-resolved measurements of the spontaneous emission visualizes these bands over the relevant $(\omega, k_{\parallel})$ range. The observed bands are accurately described by a simple coupled-wave model, which enables us to quantify the backwards and right-angle scattering of SPs at the holes in the metal film.

## 2.1 Introduction

Surface plasmons are intrinsically lossy due to the ohmic losses of the metals at which these optical excitations occur. To better harvest the unique properties of surface plasmons, in particular their compact (sub-wavelength) size, it would be great if we could compensate their losses with a nearby gain medium. Successful loss compensation enables lossless plasmonics and surface plasmon lasing [38]. This feat has been accomplished in various geometries, ranging from metal-coated nanopillars [22], to metal-coated nanorings [39] and nanowires on a silver film [23]. The common denominator in these experiments is the use of semiconductor gain media, as these media can provide huge gain. This gain is typically provided at infrared and telecom wavelengths, where surface plasmons are less confined, more photonic, and thus less lossy than in the visible range. Alternative laser medium like dyes can supply enough gain to compensate the losses of special SP excitations, like long-range surface plasmons [40] and resonances in plasmonic nanoparticle arrays [28].

Surface plasmons play a dominant role in the optical excitation and transmission of metal films perforated with a regular lattice of sub-wavelength holes, the so-called metal hole arrays. In 1998, the optical transmission of these arrays was found to be extra-ordinary large [18] on account of the resonant excitation of surface plasmons (SP). Many experiments have followed since, aimed to unravel the intriguing properties of SPs propagating and scattering on these arrays [41–44].

The periodic nature of a metal hole array, which provides distributed feed-back through scattering, is ideally suited for the construction of a plasmonic laser. Plasmonic crystal lasing was first demonstrated at mid-infrared wavelengths in quantum cascade lasers [45]. Very recently, it was also demonstrated at telecom wavelength (1.5 µm) in loss-compensated hole arrays in a gold-semiconductor structure [20]. Surface plasmon lasing was observed and three experimental proofs were reported to demonstrate the surface plasmon character of the lasing mode [20]. These experiments were performed on square arrays with a lattice spacing comparable to the SP wavelength, i.e. in so-called second-order Bragg structures.

In this chapter, we expand on the results reported in [20] by presenting a systematic study of surface plasmon lasing in a series of 9 square hole arrays with different lattice spacings and hole sizes. We compare their laser characteristics, such as emission wavelengths, lasing thresholds, and the remarkable donut-shaped modes in which these lasers emit. We focus on the angular and wavelength dependence of the luminescence that they emit, both below and above their lasing threshold. This luminescence is shown to be concentrated in four plasmonic bands, similar to the photonic bands that exist in photonic crystals. The observed shape/dispersion of these plasmonic bands can be well described with a simple coupled-mode model of four traveling SP waves that are coupled by SP-SP scattering and emit into a fifth free-space (= photonic) mode by SP-photon scattering. By analyzing these plasmonics bands for a series of devices, we present the first performance overview

of surface plasmon lasing in metal hole arrays.

## 2.2 Experimental setup

Figure 2.1(b) shows the layer package of all studied devices. This package comprises a 105 nm thick $In_{0.53}Ga_{0.47}As$ (gain) layer grown lattice-matched on a 300 μm thick double-polished InP wafer and capped with a 100 nm gold layer on top. A thin (15-20 nm) spacer layer, comprising $SiN_x$ and InP and a very thin sticking layer ($\sim 0.5$ nm chromium), in between the gold and the $In_{0.53}Ga_{0.47}As$ layer prevents quenching of the excited carriers [46]. A 20 nm thick chromium layer on top of the gold damps SPs at the gold-(chromium)-air interface. The red curve in Fig. 2.1(b) shows the square of the magnetic field profile associated with the surface plasmons at the gold-(spacer layer)-semiconductor interface. The presence of the spacer layer, with its lower refractive index, widens this profile somewhat and decreases the effective index of the SP mode, compared to that of SPs on a gold-semiconductor interface without spacer layer.

A square lattice of circular holes is patterned into the gold by a standard lift-off process that uses an array of pillars defined by e-beam lithography in a 400 nm thick layer of HPR504 resist capped with a 80 nm layer of HSQ resist. The relevant lattice spacings in our square arrays are $a_0 = 450$ nm, 460 nm, and 470 nm. For each lattice spacing we produced arrays with different hole size, by fine-tuning the e-beam dose in steps of 10%, which we denote as $d1$, $d2$, and $d3$ for increased dose and hole diameter. Each of these $3 \times 3 = 9$ arrays was produced as a $50\,μm \times 50\,μm$ pattern.

Figure 2.1(a) shows our experimental geometry. The $In_{0.53}Ga_{0.47}As$ active/gain layer is optically excited through the InP substrate, using a continuous-wave Nd:YAG laser (wavelength 1064 nm) that is spatially filtered with a pinhole and imaged into a circular top-hat shape with a diameter of $\sim 49$ μm. This beam diameter is larger than the $\sim 30$ μm reported in [13] because we now use a $f = 75$ mm lens instead of a $f = 50$ mm lens to focus the pump light. The fluorescence and laser radiation produced by the sample is observed on the gold side, using a far-field imaging system that enables us to measure the emitted intensity $I(\theta_x, \theta_y; \lambda)$ as a function of emission angle $\boldsymbol{\theta} \equiv (\theta_x, \theta_y)$ and vacuum emission wavelength $\lambda$. More specifically, the light emitted through the cryostat window is first collimated by a 20x microscope objective with a numerical aperture of 0.4, is then focused by an $f = 20$ cm (tube)lens to produce a 20x direct image of the source, and is finally reconverted into a far-field image by an $f = 5$ cm lens. We measure the far-field intensity $I(\theta_x, \theta_y; \lambda)$ by scanning a single-mode fiber in the focal plane of the final lens and analyzing the collected spectrum with a grating spectrometer. The cryostat window (0.5 mm AR-coated BK7) is thin enough to limit spherical and other optical aberrations in the imaging system. The full imaging system has an angular resolution of $\sim 4$ mrad and a wavelength resolution of $\sim 1$ nm.

The sample is operated at cryogenic temperatures in a Helium flow cryostat. The
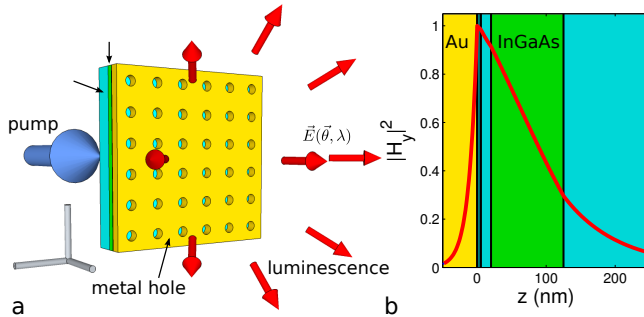
**Figure 2.1:** (a) Sketch of experimental geometry. We optically excite the gain layer through the substrate, using a continuous-wave pump laser, and observe its fluorescence and laser emission on the metal size, as a function of emission angle and wavelength. (b) The layer package of all samples consists of InP substrate, an $In_{0.53}Ga_{0.47}As$ gain layer, a thin spacer layer, and gold on top (see text for details). The red curve shows the calculated (square of the) magnetic field $|H_y|^2$ of the surface plasmon polaritons, which are excited by fluorescence, amplified by stimulated emission, and scattered by the holes.

base temperature of the cryostat is 8 K. Based on a simple model of pump-induced heating we estimate the temperature difference between the pumped region and the rest of the wafer to be limited to 5 K at 125 mW pump power. This value is small, primarily because the heat conductivity of InP is extremely large at cryogenic temperatures, with a local maximum around 20 K and heat conductivities exceeding $10^3$ W/Km between 8 and 45 K [47]. The thermal contact between the InP wafer and the rest of the cryostat might be limiting though. An indication that this is indeed the case is that the SP laser power decreases in the first few second after switch-on.

## 2.3 Angle-dependent spectra

The optical characteristic of one of our structures, with lattice spacing $a_0 = 470$ nm and hole size $d_2$, has already been reported in [20]. This device exhibits a clear lasing threshold with intense directional emission in a narrow spectral band above the lasing threshold. Below the lasing threshold, the wavelength-dependent far-field emission pattern $I(\theta_x, \theta_y; \lambda)$ provides insight on the nature of the optical excitation. Three experimental proofs were presented to substantiate the claim that lasing occurs in the surface plasmon mode: *(i)* all emission patterns can be modeled with a single effective index $n_{eff}$ with a value comparable to that expected for the only guided wave, being the SP, *(ii)* laser emission occurs in a remarkable donut-shaped beam with the radial polarization expected for SPs, being TM waves, and *(iii)* the coupling between the traveling waves, observable as avoided crossings

in the $(\omega, k_\parallel)$ dispersion, is as large as expected for SPs. In this chapter we will apply similar analysis tools to our full set of $3 \times 3$ structures.
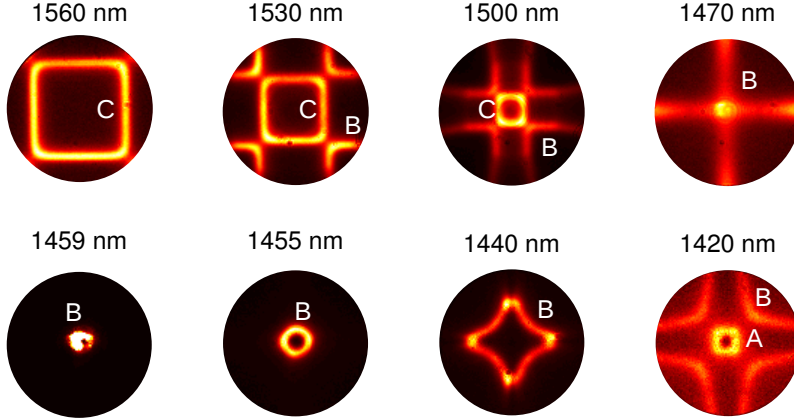


**Figure 2.2:** Far-field emission pattern of ($a_0 = 450$ nm, d2) laser observed within the NA=0.4 of our microscope objective at detection wavelengths ranging from 1560 to 1420 nm. The emission features can be divided in three groups: a low-frequency ($C$), mid-frequency ($B$), and high-frequency ($A$).

Figure 2.2 shows the far-field emission patterns $I(\theta_x, \theta_y; \lambda)$ of one of our lasers ($a_0 = 450$ nm, $d_2$) at eight selected emission wavelengths, observed under our "standard excitation condition" ($P = 125$ mW in a 49 μm diameter disk). The wavelength decreases, i.e. the optical frequency increases, from left to right and top to bottom. All patterns exhibit the 4-fold rotation and $(x, y)$ mirror symmetry expected for square arrays. For decreasing wavelength, the observed structures first move inwards and then move outwards again. The false-color scale varies from picture to picture, being normalized at the individual peak intensities, which increase from 2 at $\lambda = 1560$ nm to 10 at $\lambda = 1500$ nm, peaks at a saturated value $\gg 60$ at the lasing wavelength of $\lambda = 1459$ nm, and decreases to 9 at $\lambda = 1455$ nm and to 0.9 at $\lambda = 1420$ nm (all in arbitrary units).

The emitted structures depicted in Fig. 2.2 can be directly interpreted as equifrequency contours of the plasmonic bandstructure. The observed structures can be divided into three groups, each of which can be assigned to a specific plasmonic band. We have labeled these bands as $A$, $B$, and $C$ from high to low frequency. The $C$ band starts as a large square with rounded corners at $\lambda = 1560$ nm and shrinks to disappear between 1500 and 1470 nm. The wavelength dependence of the $B$ band is more complicated. The $B$ band is visible in the four corners at

$\lambda = 1530$ nm, transforms into a full cross at 1470 nm, then turns into a small circle at $\lambda = 1459$ nm, and grows into a larger circle at 1455 nm that transforms into a star at 1440 nm and a larger open star at 1420 nm. The $A$ band starts as a small square at $\lambda = 1420$ nm and increases in size towards lower wavelengths (not shown). Our $(a_0 = 450$ nm, $d2)$ device lases in the $B$ band at a lasing wavelength of $\lambda = 1459$ nm, where the false-color image is a saturated white. In contrast, the $(a_0 = 470$ nm, $d2)$ array studied in [20] lased in the $A$ band at $\lambda = 1479$ nm.

It is instructive to compare the patterns in Fig. 2.2 with a similar set of patterns obtained for the $(a_0 = 470$ nm, $d2)$ laser and displayed as Fig. 3 in [20]. The two sets are comparable, but the wavelengths at which similar features appear are red-shifted by approximately 4.5 % in the $a_0 = 470$ nm laser on account of the larger lattice spacing. Hence, the patterns displayed in [20] show more of the $A$ band. A closer comparison between our Fig. 2 and Fig. 3 in [20] also shows subtle differences. For instance, (i) our 4-lobed star at $\lambda = 1440$ nm has intensity maxima at its tips, whereas the 4-lobed star at 1500 nm for the $a_0 = 470$ nm device has intensity minima at its tips, and (ii) the compact structure of the $A$ band that we observe at $\lambda = 1420$ nm looks like a square, whereas a similar structure observed at 1480 nm for the $a_0 = 470$ nm device resembles a circle. Figure 2.2 thus presents a wealth of information that provides insight on the influence of SP-SP scattering on the plasmonic bandstructure.

## 2.4 Comparison of nine surface-plasmon lasers

In the rest of this chapter we will limit the discussion of the angle dependent fluorescence spectrum $I(\theta_x, \theta_y; \lambda)$ to its $\theta_y$ dependence, i.e. we fix $\theta_x = 0$. For this purpose, we combine the angular and spectral profile $I(\theta_x = 0, \theta_y; \lambda)$ in a single false-color dispersion plot. In the experiment, this plot is recorded by taking only a one-dimensional angular scan at fixed $\theta_x = 0$.

The intensity profile $I(0, \theta_y; \lambda)$ enables us to visualize the plasmonic bands of the SPs on the hole array. By choosing the angle $\theta_y$ as horizontal axis and the wavelength $\lambda$ in inverted order as vertical axis, the resulting figure closely resembles the standard $(\omega, k_{\parallel})$ dispersion diagram, where $\omega = 2\pi c / \lambda$ is the optical frequency and $k_{\parallel} = k_y = (2\pi / \lambda) \sin(\theta_y)$ is the photon momentum parallel to the interface.

Figure 2.3 shows the measured intensities $I(0, \theta_y; \lambda)$ for each of our $3 \times 3 = 9$ samples, under identical pump conditions ($P = 125$ mW in a 49 µm disk). A polarizer was inserted to single out the vertical ($=$ p $=$ TM) polarization and thereby limit the number of photonic bands from 4 to 3 (see Sec. 2.5). The data in Fig. 2.3 is arranged in a rectangular grid. The hole size increases from left to right ($d1 - d3$) and the lattice spacing increases from top to bottom ($a_0 = 450, 460$, and 470 nm). All figures have the same scale, $\theta_y = -0.4$ to 0.4 rad and $\lambda = 1400$ to 1600 nm, indicated only in the top-left figure. Each figure contains all three photonic bands ($A$, $B$, and $C$), albeit at different wavelengths and with different intensities.
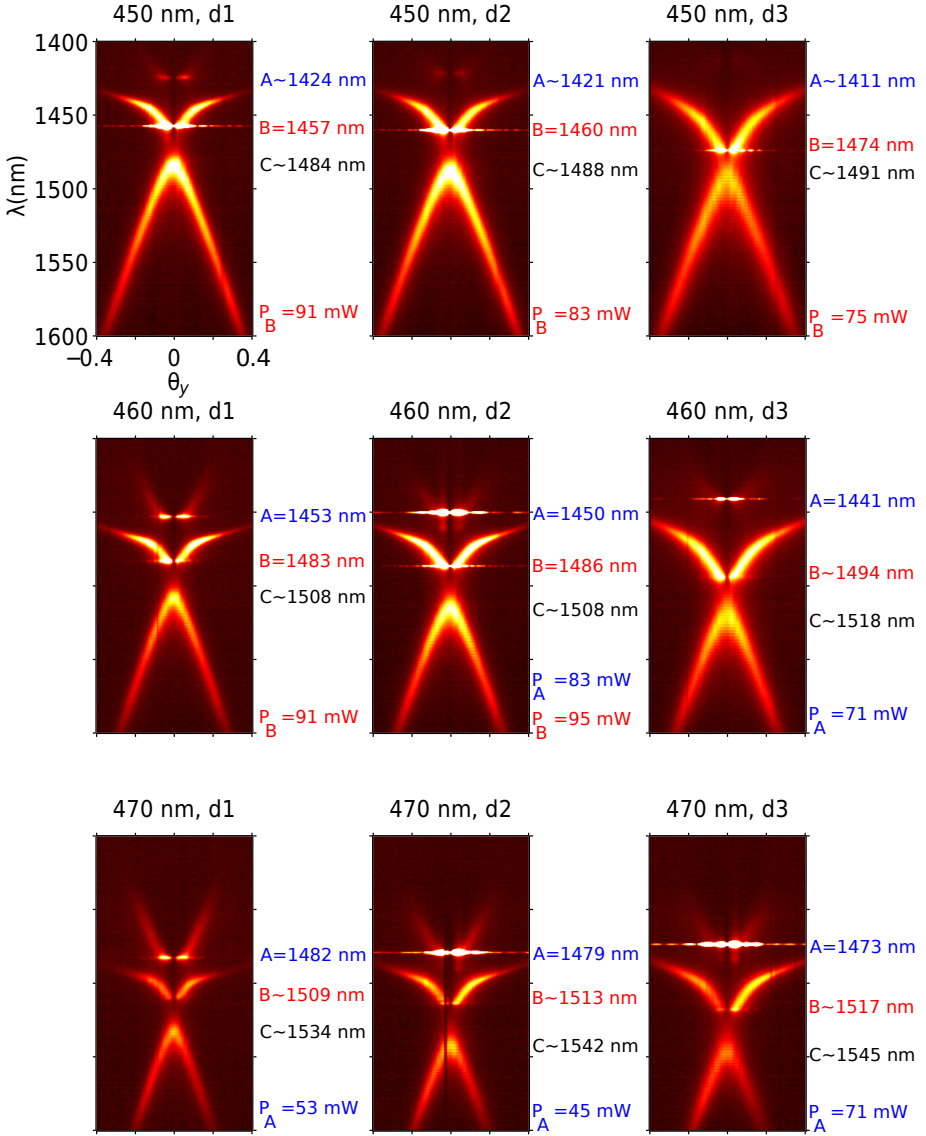
**Figure 2.3:** False-color images of the measured far-field intensities $I(0, \theta_y; \lambda)$ of our devices, which vary in lattice spacing (top to bottom; indicated in nm), and hole size (left to right; indicated as d1-d3). Lasing is visible as a saturated white, which often turns into a saturated stripe. The scale in all figures runs from $\theta_y = -0.4$ to $0.4$ mrad and from $\lambda = 1400$ to $1600$ nm and is indicated only in the top left figure. The inverted vertical axis helps to compare these figures with the standard $(\omega, k_\parallel)$ dispersion diagrams. The righthand side of each figure contains information on the wavelengths of the $A$, $B$, and $C$ bands close to normal incidence and the pump threshold of lasing modes. Note the color coding of the three bands.

15

The wavelengths around the $\theta_y = 0$ center of each band ($\theta_x = 0$ in all scans) is added on the righthand side of each figure, and denoted for instance as $B = 1457$ nm when lasing occurs in the $B$ band and as $A \sim 1424$ nm when the $A$ band only contains fluorescent emission in a somewhat wider spectral band.

When comparing the 9 pictures in Fig. 2.3, the first thing we notice is their similarity. Moving from lattice spacing $a_0 = 450$ down to 460 and 470 nm (top to bottom), all features shift downwards, such that the ratio $\lambda/a_0$ remains approximately constant. This certainly applies to the $A$ band at hole size $d1$, where the ratio $\lambda_A/a_0 = 3.16$, 3.16, and 3.15 for $a_0 = 450, 460$, and 470 nm, respectively. It is less valid for the $C$ band in this series, for which $\lambda_C/a_0 = 3.30$, 3.28, and 3.26, respectively.

The next thing we notice is that the frequency splitting between the resonances increases when the hole size increases (from left to right). More specifically, for the $a_0 = 450$ nm device we find $\lambda_A - \lambda_C = 60$ nm for hole size $d1$, 67 nm for $d2$, and 80 nm for $d3$, making the relative splitting $\Delta\lambda_{AC}/\overline{\lambda}_{AC} \equiv 2(\lambda_A - \lambda_C)/(\lambda_A + \lambda_C) = 0.041$, 0.046, and 0.055, respectively. Similar numbers apply to the lattice with $a_0 = 460$ nm, where we find $\Delta\lambda_{AC}/\overline{\lambda}_{AC} = 0.037$, 0.039, and 0.052, and to the 470 nm devices, where we find $\Delta\lambda_{AC}/\overline{\lambda}_{AC} = 0.034$, 0.042, and 0.048, respectively. All numbers are accurate to $\pm 0.001$. The increased splitting between the $A$ and $C$ bands is accompanied by a downwards shift of the $B$ band towards the $C$ band, as if the $A$ and $B$ bands repel each other. The coupled-mode model introduced in Sec. 2.5 explains both effects as an avoided crossing of photonic bands, induced by SP-SP scattering at the holes. The observed splittings are consistent with a picture where the radiative splitting increases monotonously with the ratio $d/\lambda$ probed in the experiment.

Another thing to note is the different appearance of the three photonic bands. While the low-frequency $C$ band has the more or less standard form of two straight lines, connected and capped by a smooth top, the $B$ and the $A$ band have a more intriguing angle dependence. Both bands are visible only away from the surface normal at $\theta \neq 0$. The $B$ band starts off with an almost linear dispersion that quickly levels off, while the $A$ band resembles two straight lines that loose their intensity before they meet.

All 9 studied devices exhibit laser action at the investigated pump power of 125 mW in a 49 $\mu$m disk, corresponding to a pump density $P/\text{Area} = 6.6$ kW/cm$^2$, but the lasing thresholds, at which an intense sharp spectral feature appears, differ. These threshold powers are indicated by $P_A$ and $P_B$ for laser action in the $A$ and $B$ band, respectively. The ($a_0 = 460$ nm, $d2$) device lases in both bands, seemingly simultaneously but probably in an alternating way. Under slightly different alignment, this behavior was also observed for the ($a_0 = 450$ nm, $d1$) and ($a_0 = 450$ nm, $d2$) devices, but not indicated here. The ($a_0 = 470$ nm) devices have the lowest thresholds, which starts at 53 mW for the $d1$ laser, decreases to 45 mW for the $d2$ laser, and increases to 71 mW for the $d3$ laser. This variation indicates that there is an

optimum hole size for surface plasmon lasing.

The accuracy of the threshold measurements is limited to ±20%, as the lasing threshold depends on the location of the 49 μm round pump spot within the 50 μm square array. For all devices, laser action typically occurred over the full pumped area, but the emission was seldom spatially uniform over this area and for some devices it was clearly concentrated at the edges of the array. These spatial observations were made with an infrared CCD illuminated with a magnified direct image of the devices.

Lasing in either the *A* or *B* band occurs at comparable threshold powers. None of the studied devices lased in the *C* band, nor did this laser action occur in a similar set of devices with lattice spacing $a_0 = 440$ nm, where the *C* band was shifted upwards in the figures to a resonance wavelength of $\lambda_C \approx 1462$ nm, more in line with the lasing wavelengths of the other devices.

Each lasing device emits its light in a remarkable beam profile that is approximately donut-shaped, radially polarized, and centered around the surface normal [20]. Although this statement applies to all lasers, the angular widths of the emitted donut beams are noticeably different. The beams emitted in the *A* band typically have an angular diameter of $\Delta\theta \approx 65 \pm 6$ rad. The beams emitted in the *B* band are less collimated, with typical diameters of $\Delta\theta \approx 85 \pm 8$ rad. This diameter is comparable to the diameter of $\Delta\theta \approx 90 \pm 10$ rad (FWHM 120 rad [20]) measured for the same laser under excitation with a 2/3× smaller pump spot. There is, apparently, no simple (Fourier) relation between these opening angles $\Delta\theta$ and the size of the pump spot. Furthermore, the product of opening angle times pump size is considerably larger than the value expected from Fourier relations.

After the optical inspection presented above, we took the sample out of the cryostat and placed it in a scanning electron microscope (SEM) for inspection and an experimental estimate of the hole diameters. This inspection showed that the holes were nicely circular and uniform (standard deviation in hole size 1-2%). The measured hole diameters $d$ are: (180, 179, and 175 nm) for $d1$, (189, 187, and 183 nm) for $d2$, and (221, 206, and 202 nm) for $d3$, where the numbers in parentheses refer to the samples with lattice spacings $a_0 = (450, 460, 470$ nm). As expected, the hole diameter increases with e-beam dose and increases slightly with decreasing $a_0$ due to proximity effects.

## 2.5 Coupled-mode model

This theoretical section presents a relatively simple coupled-mode model for the observed angular emission spectrum $I(0, \theta_y; \lambda)$ and the associated plasmonic bands. Before doing so, we first note that the highly directional nature of the observed spectrum is not as straightforward as one might think. On the contrary: we expect the direct fluorescent photon emission through the holes to be spread out over all angles, because each sub-wavelength hole radiates like a dipole and because radiation from neighboring holes should hardly be correlated, as the fluorescent

medium is thin in relation to the hole spacing. The observed directionality of the emission, on the other hand, proofs the existence of long-range coherence between the emitting holes. This coherence must be created by traveling-wave surface plasmons that are excited by fluorescence and later converted into photons by coherent scattering on the holes in the lattice. More specifically, most photons emitted at an angle $(\theta_x, \theta_y)$, with an associated photon momentum $\mathbf{k}_\| \equiv (k_x, k_y)$ with $k_x = (2\pi/\lambda)\sin\theta_x$ and $k_y = (2\pi/\lambda)\sin\theta_y$, originate from coherent scattering of traveling-wave SPs with momenta $\mathbf{k}_{sp} = \mathbf{G}_i + \mathbf{k}_\|$, where $\mathbf{G}_i$ is a lattice vector. For our device, which has modest scattering and operates close to the 2nd-order Bragg condition $k_{sp} \equiv |\mathbf{k}_{sp}| \approx 2(\pi/a_0)$ only four SP traveling waves are important. These corresponds to the four fundamental lattice vectors with $|\mathbf{G}_i| \equiv G = (2\pi/a_0)$, pointing in the four lattice directions $\{\mathbf{e}_x, \mathbf{e}_{-x}, \mathbf{e}_y, \mathbf{e}_{-y}\}$. We will thus denote them as the $+x, -x, +y,$ and $-y$ traveling waves, although strictly speaking their wavevector might deviate slightly from these directions when $k_\| \neq 0$ ($k_\| \ll G$).

A first-order approximation of the dispersion of the SP bands neglects the influence of scattering and simply uses the dispersion relation $\omega = |\mathbf{k}_{sp}|c/n_{eff}$ of traveling-wave SPs on a smooth metal-dielectric interface, where $n_{eff}$ is the SP effective index. We only consider angle-tuning in the $yz$-plane, where $\mathbf{k}_\| = k_\| \mathbf{e}_y$, and use the paraxial (= small-angle) approximation to write $k_\| \approx (2\pi/\lambda)\theta_y$. In the equations presented below, we will abbreviate $\theta_y$ as $\theta$ and often use the approximation $(2\pi/\lambda) \approx (2\pi/\lambda_0)$ for the mentioned prefactor, where $\lambda_0 = 2\pi c/\omega_0 \equiv n_{eff}a_0$ is a fixed reference wavelength, as wavelength variations within the SP bands are small ($\lambda \approx \lambda_0$). Under these conditions, it is easy to show that the eigenfrequencies of the two $\pm y$ modes are $\omega(\theta) = k_{sp}(\theta)c/n_{eff} = (G \pm k_\|)c/n_{eff} \approx \omega_0 \pm c_1\theta$, with $c_1 \equiv \omega_0/n_{eff}$. The uncoupled $\pm y$ modes thus exhibit a linear dispersion, which can also be written as $\lambda(\theta)/a_0 = n_{eff} \pm \theta$ if we stick the original form $k_\| = (2\pi/\lambda)\theta$. The eigenfrequencies of the two $\pm x$ modes are both $\omega(\theta) \approx \omega_0 + c_2\theta^2$, with $c_2 \equiv \omega_0/(2n_{eff}^2)$, as the SP wavevector of these modes $k_{sp}(\theta) = \sqrt{G^2 + k_\|^2} \approx (2\pi/\lambda_0)\sqrt{n_{eff}^2 + \theta^2}$, with $\sqrt{n_{eff}^2 + \theta_y^2} \approx n_{eff} + \theta^2/(2n_{eff})$. The dispersion relations of these four uncoupled traveling SP waves are depicted in Fig. 2.4(a).

In our system, the uncoupled traveling-wave model is accurate enough only at angles sufficiently far away from the surface normal, where it produces the piecewise circular dispersion contours depicted in Fig. 2 of [20]. At smaller momenta $\mathbf{k}_\|$, the scattering-induced interaction between the (now almost frequency-degenerate) SP waves needs to be included. We do so with a coupled-mode model that decomposes the SP field at any position $\mathbf{r} \equiv (x, y)$ in its traveling-wave components

$$\mathbf{E}(\mathbf{r}, t) = \left[ E_x(t)\mathbf{u}_x e^{iGx} + E_{-x}(t)\mathbf{u}_{-x}e^{-iGx} + E_y(t)\mathbf{u}_y e^{iGy} + E_{-y}(t)\mathbf{u}_{-y}e^{-iGy} \right]e^{ik_\| y},$$
$$(2.5.1)$$

where $\{E_x, E_{-x}, E_y, E_{-y}\}$ are the modal amplitudes of the four traveling waves and $\mathbf{u}_i$, with $i = \{x, -x, y, -y\}$, are unit vectors that describe the four associated optical polarizations. We choose these eigenvectors to be rotationally-imaged copies of each
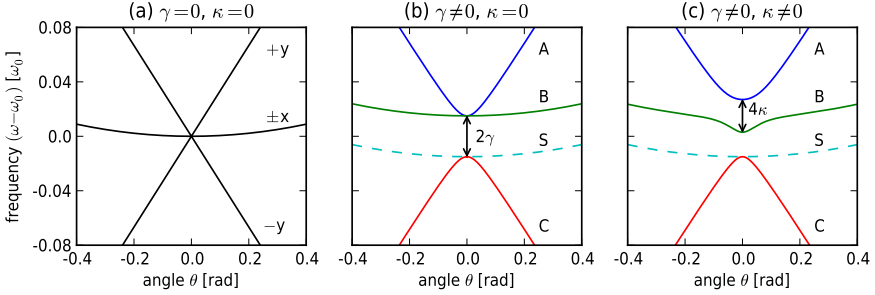
**Figure 2.4:** Dispersion curves of the four SP bands, depicted as frequency difference ($\omega - \omega_0$) versus angle $\theta$, for three different models of increasing complexity: (a) uncoupled traveling waves, (b) backscattering only, and (c) right-angle and backscattering. Fig. (a) shows the linear dispersion of the $\pm y$ modes at slope $\pm c_1 = 1/n_{\text{eff}}$, for $n_{\text{eff}} = 3$ and the almost flat-band dispersion for the $\pm x$ modes. Fig. (b) shows the case $\gamma/\omega_0 = 0.015$, where the $\pm y$ bands exhibit an avoided crossing at $\theta = 0$ and where the $\pm x$ bands have a fixed splitting $2\gamma$. The three solid bands $A$, $B$, and $C$ couple to $p$-polarized light, whereas the single dashed $S$ band couples to $s$ polarization. Fig. (c) shows how only the cosine-type modes exhibit a second avoided crossing around $\theta = 0$ when right-angle scattering at a rate $\kappa/\omega_0 = 0.006$ is added.

other, such that the perpendicular component $E_\perp$ of their electric fields are in phase if the modal amplitudes are. Equation (2.5.1) is the Bloch-mode representation of the relevant SP field, in first-order Fourier components only. When the four modal amplitudes are combined into a single vector $E$, the time evolution of this SP field can be expressed as $dE/dt = -iHE$, where $H$ is a $4 \times 4$ matrix. If scattering is neglected, $H$ reduces to a diagonal matrix with the elements/eigenvalues mentioned above, being $\{\omega_0 + c_2\theta^2, \omega_0 + c_2\theta^2, \omega_0 + c_1\theta, \omega_0 - c_1\theta\}$.

The effects of SP scattering can be easily incorporated in the matrix description. The 4-fold rotation and $(x, y)$ mirror symmetry of the square lattice enables us to divide the SP-SP scattering in three fundamental processes: forward scattering under 0°, right-angle scattering under ±90°, and backwards scattering under 180°. Forward scattering at a rate $\gamma_0$ merely changes the eigenfrequencies of all traveling waves, but does not couple these waves. It can thus be easily incorporated in our model by redefining the combination $\omega_0 + \gamma_0$ as the new $\omega_0$, which simply indicates that the effective index $n_{\text{eff}}$ of SPs on a surface with holes can be different than that of SPs on a smooth surface. Backwards scattering couples the $x \leftrightarrow -x$ and $y \leftrightarrow -y$ waves at an amplitude scattering rate $\gamma$. Right-angle scattering leads to coupling between the $\pm x \leftrightarrow \pm y$ traveling waves at an amplitude scattering rate $\kappa$.

Inclusion of all coupling rates into our $dE/dt = -iHE$ matrix description yields

$$
H = \begin{pmatrix}
\omega_0 + c_2\theta^2 & \gamma & \kappa & \kappa \\
\gamma & \omega_0 + c_2\theta^2 & \kappa & \kappa \\
\kappa & \kappa & \omega_0 + c_1\theta & \gamma \\
\kappa & \kappa & \gamma & \omega_0 - c_1\theta
\end{pmatrix}
\tag{2.5.2}
$$

Although the presented model is very general and can be applied to plasmonic as well as photonic crystals [48] it contains one central assumption that needs to be discussed. For simplicity, we have chosen the coupling rates $\gamma$ and $\kappa$ to be real-valued, making the coupling conservative and $H$ Hermitian. However, being amplitude scattering rates, $\gamma$ and $\kappa$ do not need to be real-valued [49]. They could in principle contain imaginary parts, which would then result in dissipative coupling and (mode-selective) energy loss. Although a future and more detailed analysis will probably show that these imaginary parts are not strictly zero, we prefer the simplicity for now. We can also justify this simplification with two arguments. First of all, theory predicts that small ($\ll \lambda$) holes scatter light in an off-resonant way, such that both the polarizability and the related scattering rates $\gamma$ and $\kappa$ are real-valued [50]. Secondly, previous experiments on SPs on an air-metal interface with a grid of 50 nm wide slits measured conservative coupling to dominate over dissipative coupling at a normalized rate of $\gamma/\omega_0 = 0.022$ versus 0.008 for the mentioned geometry [51].

The plasmonic bands of our system are associated with the eigenvalues of the $H$ matrix. As these are quite complicated, we will first consider a simpler system without right-angle scattering, i.e. with $\kappa = 0$, where the $H$ matrix separates in two $2 \times 2$ blocks. The lower ($y$) block describes the prototype avoided crossing with eigenvalues $\omega(\theta) = \omega_0 \pm \sqrt{\gamma^2 + (c_1\theta)^2}$. The associated eigenmodes are $(1, \pm 1)$, with corresponding field profiles $E(\mathbf{r}) \propto \cos Gy$ and $E(\mathbf{r}) \propto \sin Gy$, at $\theta = 0$, and an unbalanced superposition of traveling waves at $\theta \neq 0$. The upper ($x$) block has eigenvalues $\omega(\theta) = \omega_0 + c_2\theta^2 \pm \gamma$. Its eigenmodes are $(1, \pm 1)$, with corresponding field profiles $E(\mathbf{r}) \propto \cos Gx \cdot \exp ik_y y$ and $E(\mathbf{r}) \propto \sin Gx \cdot \exp ik_y y$, at any $\theta$. These results are depicted in the four dispersion curves in Fig. 2.4(b).

The general case also contains right-angle scattering ($\kappa \neq 0$), which couples the $\pm x \longleftrightarrow \pm y$ traveling waves and thereby complicates the model. Before we resort to numerics, we like to point out that our 4 mode model is actually a 3+1 mode problem. The $(1, -1, 0, 0)$ eigenmode, with eigenvalue $\omega_0 + c_2\theta^2 - \gamma$, is special as it doesn't change with angle and is not affected by right-angle scattering. The physical reason for this is that the $E_0(\mathbf{r}) \propto \sin Gx \cdot \exp ik_y y$ profile of this mode doesn't scatter, because it has intensity minima at the holes, or - phrased in a different way - because the scattering contributions from the two counter-propagating waves interfere destructively. Below, we will argue that this special SP eigenmode is the only mode that emits s-polarized light.

The three remaining SP waves form a coupled set, of which the solution is only

simple at $\theta = 0$, where the $(0, 0, 1, -1)$ eigenmode, with $E_1(\mathbf{r}) \propto \sin G y$ profile, then has the same eigenvalue $\omega_0 - \gamma$ as the $(1, -1, 0, 0)$ mode. At $\theta = 0$, the two cosine-type standing waves $\cos G x$ and $\cos G y$ couple into two eigenmodes of the form $E_{2,3}(\mathbf{r}) \propto \cos G x \pm \cos G y$, with eigenvalues $\omega_0 + \gamma \pm 2\kappa$. At $\theta \neq 0$, they also couple to the $E_1(\mathbf{r})$ mode and the eigenvalue problem now corresponds to finding the roots of a third-order polynomial. Figure 2.4(c) shows the numerically obtained results for the realistic case $\kappa/\gamma = 0.4$.

## 2.6 SP-photon coupling and vector aspects

It is good to know the SP eigenmodes, but this is not yet the complete story. As the observed fluorescence originates from coherent scattering of the four SP traveling waves, its intensity depends crucially on the (far-field) interference between these scattering contributions. Constructive interference can make some SP modes bright (= radiative), whereas destructive interference can make other SP modes practically invisible (= non-radiative). This phenomenon is clearly visible in Fig. 2.3, where the $A$ and $B$ bands loose their intensity around $\theta = 0$, whereas the $C$ band still radiates.

We also need to consider the vector character of the electro-magnetic fields, which is hidden in the eigenvectors $\mathbf{u}_i$ of the SP waves. By solving Maxwell's equations at a metal-dielectric interface, one quickly finds that each SP traveling wave contains three field components, just like any TM-mode in a planar medium: an in-plane magnetic field $H_\parallel$, perpendicular to the propagation direction, an out-of-plane electric field $E_\perp$, and an in-plane electric field $E_\parallel$ in the direction of $\mathbf{k}_{\text{sp}}$, which for the SP is much weaker than $E_\perp$ and approximately 90° out of phase with the other two field components. The interference between two counter propagating SP waves depends on the field component that we consider. When the out-of-plane electric field components $E_\perp$ interfere constructively, to produce a cosine-type pattern, the two in-plane field components $E_\parallel$ and $H_\parallel$ interfere destructively, into a sine-type pattern, and vice versa. This difference will play a crucial role in the comparison between theory and experiment.

The vector character of the SP field determines the polarization of the emitted light. Instead of discussing the vectorial aspects of the SP-photon scattering, this can also be understood from symmetry, which, for emission at $\theta_x = 0$ is the mirror symmetry in the $yz$ (emission) plane. For TM-polarized waves, the four eigenmodes naturally divide in three vectorial modes that are even under mirror action and therefore only couple to $p$-polarized light and one mode that is odd and only emits $s$-polarization [48]. To understand why, let's consider the symmetry of the $H$ field of the four standing waves. The two linear combinations of the $\pm y$ SPs, with magnetic fields $\mathbf{H}(\mathbf{r}) \propto \sin G y \cdot \exp i k_\parallel y \, \mathbf{e}_x$ and $\cos G y \cdot \exp i k_\parallel y \, \mathbf{e}_x$, are both even under mirror action, as their field profiles are even and the magnetic field is a pseudovector, and therefore emit $p$ (TM) polarized light in the $yz$ plane. The two linear combinations of the $\pm x$ SPs combine SPs with $\mathbf{k}_{\text{sp}} = \pm G \mathbf{e}_x + k_\parallel \mathbf{e}_y$ and

therefore have $\mathbf{H}$ components in both the $\mathbf{e}_x$ and $\mathbf{e}_y$ direction. The combination with dominant magnetic field $H_y(\mathbf{r}) \propto \sin Gx \cdot \exp ik_\parallel y$ is even under mirror action and thus emits $p$-polarized light, albeit only through coupling with the other even SP modes. The combination with magnetic field profile $\mathbf{H}(\mathbf{r}) \propto \exp ik_\parallel y [\cos Gx \, \mathbf{e}_y - i(k_\parallel/G) \sin Gx \, \mathbf{e}_x]$ is the only combination that is odd and radiates $s$-polarized light.

The symmetry argument presented above ended with the statement that the SP standing wave with dominant magnetic field profile $H_y(\mathbf{r}) \propto \cos Gx \cdot \exp ik_y y \mathbf{e}_y$ is a 'special' eigenmode. At first sight this statement seems to be in conflict with our 3+1 coupled-mode model, where we concluded that the 'special' eigenmode has a mode profile $E_0(\mathbf{r}) \propto \sin Gx \cdot \exp ik_y y$. This paradox is solved when we realize that the cosine profiles of the in-plane $H$ fields corresponds to a sine profiles of the out-of-plane $E$ field, and vice verse. The former determines the SP-photon coupling, whereas the latter apparently dominates the SP-SP scattering. The special mode was removed in the experiment with a polarizer set for $p$ (TM) transmission.

The next step in theory could be the development of a microscopic model that explains the origin of scattering rates $\gamma$, $\kappa$, and $\gamma_0$. For small holes, this scattering is typically modeled by considering each hole as a polarizable object that scatters through dipole radiation. Under TM-polarized excitation, the induced electric dipole has both an out-plane component $p_\perp$ and an in-plane component $p_\parallel$. The induced magnetic dipole, which is unique in metals, only has an in-plane component $m_\parallel$. The orientation of these dipoles derive three general rules for the relative magnitudes of the mentioned scattering rates: (i) right-angle SP-SP scattering is only supported by the electric dipole $p_\perp$, (ii) forwards and backwards SP-SP scattering are supported by both $p_\perp$ and $m_\parallel$, albeit in different combinations ($p_\perp + m_\parallel$ versus $p_\perp - m_\parallel$), and (iii) the SP-photon scattering observed close to the surface normal is insensitive to $p_\perp$ and dominated by $m_\parallel$, as $p_\parallel$ is typically weak.

Whether the hole is small enough to validate the dipole approximation mentioned above depends on the ratio of hole radius $r$ over SP wavelength $\lambda_{sp}$. The observed hole diameters in all our sample, apart from ($a_0 = 450$ nm, $d3$), span a range $d = 2r = 175$-$206$ nm, which corresponds to dimensionless ratio's $r/\lambda_{sp} = 0.19 - 0.22$. Figure 2 in the supplementary material of [50] indicates that these ratio's are at the edge of validity range of the dipole approximation: the electrical polarizability is still dominantly real-valued, but the magnetic polarizability already has a sizeable imaginary component. Hence we expect $\kappa$ to be dominantly real-valued, whereas $\gamma$ might already have a sizeable imaginary component.

## 2.7 Comparison experiment and theory

After having presented the experimental dispersion curves in Fig. 2.3 and the theoretical curves in Fig. 2.4(c), we are finally able to compare the two. We start by noting that Figure 2.3 displays only the three $p$ (TM) polarized bands. The fourth $s$-polarized band exhibits hardly any dispersion and has a (very wide) extremum with a central wavelength that practically coincides with that of the $C$ band, as

demonstrated in Fig. 2.5 below for one of the lasers. This $s$-polarized band is without any doubt the special $E_0(\mathbf{r}) \propto \sin Gx \cdot \exp i k_y y$ band.

A qualitative comparison between the nine experimental pictures in Fig. 2.3 and the theoretical prediction in Fig. 2.4 leaves no doubt about the labeling of the $p$-polarized bands. The high-frequency band $A$ and the low-frequency band $C$ are the $\pm y$ traveling waves, with eigenvalues $\omega_0 \mp c_1 \theta$ and field profiles $E(\mathbf{r}) \propto \exp i(k_\parallel \pm G)y$ at large $\theta$, whereas the mid-frequency band is the $B$ band. This labeling is supported by two arguments. First of all, the observation that the center of the $C$ band practically coincidence with the center of the $s$-polarized band is as expected: at $\theta = 0$ these modes have the same eigenvalue $\omega_0 - \gamma$ and comparable mode profiles ($E_0(\mathbf{r}) \propto \sin Gx$ versus $E_1(\mathbf{r}) \propto \sin Gy$. The $A$ and $B$ modes, on the other hand, have different eigenvalues $\omega_0 + \gamma \pm 2\kappa$ and eigenmodes $E_{2,3}(\mathbf{r}) \propto \cos(Gx) \pm \cos(Gy)$ at $\theta = 0$.

The proposed labeling is also consistent with the radiative or non-radiative character of the eigenmodes around $\theta = 0$. The $C$ and $s$-polarized modes have a sine-type profile in $E_\perp$ and a corresponding cosine-type profile in $E_\parallel$ and $H_\parallel$, which makes them radiative modes. The $A$ and $B$ modes, on the other hand, have cosine-type profiles in $E_\perp$ and sine-type profiles in $E_\parallel$ and $H_\parallel$, and therefore do not radiate at $\theta = 0$. The $A$ and $B$ band indeed becomes extremely faint and disappears close to the surface normal. The overall labeling is also supported by optical transmission spectra, recorded with white light incident along the surface normal, which only show the resonance of the (radiative) $C$ band but not those of the (non-radiative) $B$ and $A$ bands [19].

We have fitted all 9 dispersion curves in Fig. 2.3, by looking in particular at the fit quality around $\theta = 0$. The frequency difference between the upper bands $(\omega_A - \omega_B) = 4\kappa$ at $\theta = 0$ yields the rate of right-angle scattering rate, although we do not know its sign. The frequency difference between the average of the upper two bands and the lower band $(\omega_A + \omega_B - 2\omega_C)/2 = 2\gamma$ at $\theta = 0$ yields the back scattering rate. In this case we do know the sign. The observation that the split bands lie above the degenerate bands shows that $\gamma > 0$, such that modes with a cosine-type $E_\perp$-profile have a higher resonance frequency and a larger effective index than the modes with a sine-type profile. The numbers obtained from these fits correspond to right-angle scattering rates $\kappa/\omega_0 = 0.005 - 0.011$ for increasing hole size. The backwards scattering rate $\gamma/\omega_0 = 0.013 - 0.017$ is considerable larger and increases less rapidly with hole size. Our observation that $\gamma > \kappa$ is consistent with the notion that the induced magnetic dipole $m_\parallel$, which contributes only to $\gamma$, is a stronger scatterer than the induced electric dipole $p_\perp$, which scatters in all directions. For comparison, we note that in holes in dielectric slabs, which scatter only through electric dipoles, typically yield a scattering rate $\gamma$ that is (somewhat) larger that $\kappa$, such that the special $s$-polarized band for coupled TM modes now coincides with the $B$ band instead of the $C$ band [48].

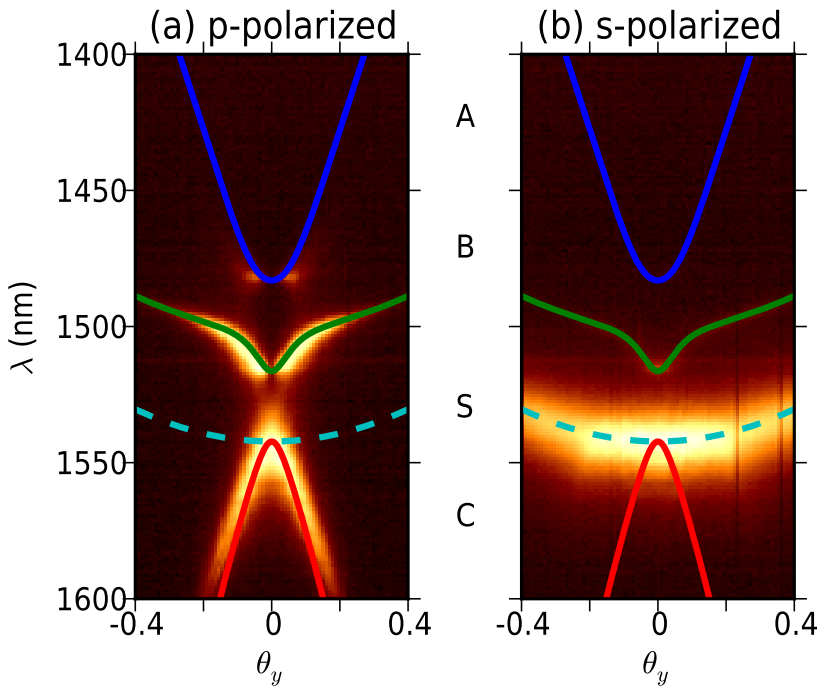Figure 2.5 shows a detailed comparison of the measurements and fits for one of

**Figure 2.5:** Dispersion curves of four SP bands of the $(a_0 = 470\ \text{nm}, d2)$ laser for (a) p-polarized and (b) s-polarized emission. The three solid and single dashed curve show the $p$-polarized $(A, B, C)$ bands and the $s$-polarized $S$ band and are calculated based on three fit parameters: $\gamma$, $\kappa$ and $n_{\text{eff}}$ (see text).

our lasers. Figure 2.5(a) and 2.5(b) show the *p*-polarized and *s*-polarized emission, respectively, of the ($a_0 = 470$ nm, $d_2$) laser (see also supplement of [20]). The combined fit, depicted as three solid curves and one dashed curve, is based on $\gamma/\omega = 0.0140$, $\kappa/\omega = 0.0056$, and $n_{\mathrm{eff}} = 3.235$, and optimized by eye. The high quality of this combined fit is typical for all studied lasers.

The most intriguing aspect of surface plasmon lasers is undoubtedly their approximately donut-shaped and radially-polarized emission. In the above discussion, we have linked the central hole in the donut to the non-radiative character of the *A* and *B* modes that these lasers operate on. An obvious question to ask, then, is whether the SP field in the laser simply avoids the fundamental wave vectors $\mathbf{k}_{\mathrm{sp}} = \mathbf{G}_i$ or whether the SP field in the laser is far more intense then we actually observe, because laser action also occurs at $\mathbf{k}_{\mathrm{sp}} = \mathbf{G}_i$, but is simply invisible as SPs in non-radiative bands barely couple to the outside world. The latter scenario is quite plausible, in particular because non-radiative modes are bound to be the first ones to lase, precise because they hardly suffer from radiation loss. Hence we expect that our SP lasers might be (much) brighter than they seem to be.

In future research, we would like to study the optical coherence within the emitted donut-like beams. We will also try to make the *C* mode lase in at least one of our devices, in order to check whether the characteristics of this radiative band are really as different as we expect them to be.

## 2.8 Conclusion

In conclusion, we have presented a systematic study of the performance of a series of semiconductor metal hole array lasers with different lattice spacings and hole sizes. Angle- and wavelength-resolved measurements of the luminescence of the $In_{0.53}Ga_{0.47}As$ gain medium provides important insight in the nature of the lasing modes and the dispersion of all surface plasmon (SP) resonances on the hole arrays. The hole arrays act as a second-order Bragg reflector that provides distributed feedback to the laser close to normal incidence. We observe four plasmonics bands, which correspond to four linear superpositions of SP traveling waves, and could identify all bands. Three bands couple to *p*-polarized light, of which only one radiates along the surface normal. One band couples to *s* polarized light and also radiates along the surface normal. A relatively simple coupled-wave model enables us to extract the amplitude rates for SP-SP scattering, both under 90° ($\kappa$) and in the backwards direction ($\gamma$). For the lasers studied in this chapter, with a hole diameter to lattice constant of $d/a \approx 0.4$, the observed plasmonic bandstructures correspond to amplitude scattering rates $\kappa/\omega_0 = 0.005 - 0.011$ and $\gamma/\omega_0 = 0.013 - 0.017$ for right-hand and backwards scattering, respectively.

## Acknowledgements